Mathematical Models of Acoustically Induced Vaporization of Encapsulated Nanodroplets

K. Jiang, M. Ghasemi, A. Yu, and S. Sivaloganathan

1 Introduction

Acoustic droplet vaporization (ADV) is a process in which droplets of liquid are vaporized through the application of ultrasound acoustic waves. Since its initial description in 1995 [8], the potential usefulness of this process within the medical field has been explored through proposed and demonstrated applications such as drug delivery, imaging, and embolic therapy.

The exploitation of this process for medical applications involves the introduction of droplets, typically several hundred nanometers in size, of an appropriately selected biocompatible organic compound into a patient's bloodstream. Ultrasound is then applied at the required site to induce the vaporization of these nanodroplets noninvasively and thus achieve the desired clinical purpose. Perfluorocarbons (PFCs) are the most explored class of compounds for this application due to their physicochemical properties, their lightest species having a boiling point below human body temperature, yet remaining metastable in the liquid state due to the additional Laplace pressure within the droplet arising from surface tension [9]. These droplets are typically encapsulated with either an albumin layer [10], a polymeric shell [12, 13], or fluorinated surfactants [14] to prevent their rapid dissolution within the bloodstream, thus improving their lifetime.

The distribution of administered drugs within the body poses a key challenge within the field of cancer chemotherapy. Severe side effects are caused by the

K. Jiang · M. Ghasemi · A. Yu
University of Waterloo, Waterloo, ON, Canada
e-mail: k27jiang@uwaterloo.ca; m23ghasemi@uwaterloo.ca; alfred.yu@uwaterloo.ca

S. Sivaloganathan (✉)
Center for Mathematical Medicine, The Fields Institute, Toronto, ON, Canada
e-mail: ssivaloganathan@uwaterloo.ca

R. P. Mondaini (ed.), *Trends in Biomathematics: Stability and Oscillations in Environmental, Social, and Biological Models*,
https://doi.org/10.1007/978-3-031-12515-7_7

cytotoxic effects of these drugs on healthy tissue. In addition, anomalous tumour vascularization and high interstitial pressure result in spatial drug gradients within a tumor, leading to the possible survival of cancer cells where drug concentration is low [15]. This challenge can be addressed through the development of targeted drug delivery techniques that increase the concentration of drugs within the tumour whilst minimizing the impact on healthy tissue. The small size of the aforementioned encapsulated nanodroplets and their stability within the bloodstream allow them to both circulate around the body and accumulate within tumour tissue through the enhanced permeability and retention (EPR) effect [16]. Targeted drug delivery can then potentially be achieved via the selective release of any encapsulated drugs by inducing ADV through the noninvasive application of a focused ultrasound field.

A limitation of conventional ultrasound imaging techniques is the difficulty encountered when imaging tissue microvasculature due to the small size of the microvessels and the poor resolution of signal between the blood and the surrounding tissue [17]. The ADV of encapsulated nanodroplets can turn them into micrometer-scale gas bubbles which oscillate under the influence of the applied acoustic field. This enhances the backscattered signal, boosting the contrast between the vasculature and the surrounding tissue, thus allowing us to overcome the above limitation [17]. The expansion in volume can also occlude blood vessels feeding a tumour, starving them of nutrients and thus damaging or eliminating them. The exploitation of this process for therapeutic benefits is known as embolotherapy [18].

The increase in stability caused by the Laplace pressure across the droplet surface, together with the encapsulating shell implies that a certain threshold of acoustic energy must be exceeded in order to achieve vaporization. The dependence of this threshold on various parameters such as acoustic frequency [11, 19, 20], pulse length [20–22], pulse repetition frequency [23], droplet size [19, 23] and concentration [22], as well as temperature [20, 22, 23] has been studied experimentally *in vitro*. A successful mathematical model of the ADV process and its dependence on some or all of the above factors can be used to optimize this process through the appropriate selection of an encapsulating shell with suitable physical characteristics, as well as the parameters of the applied acoustic field. It may also yield useful behavioural predictions in conditions that have yet to be tested experimentally.

Current physical models of ADV assume the presence of a spherical vapor bubble within the liquid droplet and an important aspect is the examination of the evolution of this bubble over time [4, 5]. Hence they build upon and incorporate early mathematical models of spherical bubble behavior. One such model is Lord Rayleigh's examination of the collapse of a spherical cavitation bubble within a liquid under constant pressure at a distance [28]. This was extended by Plesset to incorporate the possibility of time-varying external pressure [29]. The combined works form the basis of what has come to be known as the Rayleigh-Plesset framework and has since been extended further to incorporate the effects of surface tension [30], viscosity [31], heat diffusion [30, 32], and compressibility [33].

This paper presents two recent models of the ADV process. These models utilize the general Rayleigh-Plesset equation accounting for the effects of surface tension, viscosity, and heat diffusion (although still assuming incompressibility).

They also incorporate the effect of mass flux across the bubble surface through evaporation/condensation, as well as pressure contributions from the encapsulating shell. The first model, developed by Guédra et. al. [4] assumes that the shell exhibits linear elasticity. The second model, developed by Lacour et. al. [5] builds upon this by introducing nonlinear elasticity by treating the shell as a Mooney-Rivlin solid to account for large deformations.

2 Modelling

As shown in the above schematic (Fig. 1), the model represents the radius of the vapor bubble, the inner and outer radius of the shell as three concentric spheres with radii $R(t), a(t), b(t)$ respectively. It is assumed that the space within the inner vapor bubble, between the vapor bubble and the shell, and outside of the shell contains PFP vapor, liquid PFP, and water respectively. To model the evolution of these values over time, the following dynamics are taken into account:

1. Vapor behavior within the bubble
2. Mass flux and heat transfer across the bubble surface
3. Heat transfer and fluid flow within the liquid between the bubble surface and the shell
4. Heat transfer across the shell

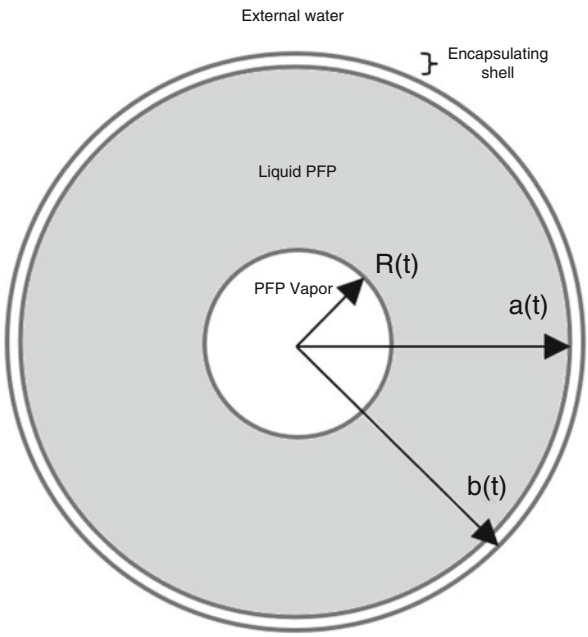

Fig. 1 Schematic of the model setup

5. Heat transfer and fluid flow within the external liquid

2.1 Evolution of Bubble Radius Over Time

The evolution of the bubble radius over time is described by the generalized Rayleigh-Plesset equation [5] which is obtained as follows. Its derivation begins with the Navier-Stokes equation for radially symmetric flows

$$-\frac{1}{\rho}\frac{\partial p}{\partial r} = \frac{\partial u}{\partial t} + u\frac{\partial u}{\partial r} - \nu\left[\frac{1}{r^2}\frac{\partial}{\partial r}\left(r^2\frac{\partial u}{\partial r}\right) - \frac{2u}{r^2}\right] \tag{1}$$

Where, ρ is the density, p is the pressure, $u := u(r,t)$ is the radial velocity at radial distance r from the bubble center at time t, and ν is the kinematic viscosity. By the conservation of mass, the radial velocity u must satisfy

$$u(r,t) = \left(\frac{R}{r}\right)^2 U(t) \tag{2}$$

Where $U(t) := \lim_{r\to R^+} u(r,t)$ is the velocity of the inner liquid right at the surface of the bubble. Plugging this into Eq. (1) results in

$$-\frac{1}{\rho}\frac{\partial p}{\partial r} = \frac{R^2\dot{U}}{r^2} + \frac{2R\dot{R}U}{r^2} - 2\frac{R^4U^2}{r^5} \tag{3}$$

Noting that the viscosity terms within the right-hand side of Eq. (1) cancel each other out as a result. (3) can then be integrated across the three domains of inner liquid $[R,a]$, shell $[a,b]$, and outer liquid $[b,\infty]$ to obtain the following [4]

$$R\dot{U} + \frac{4\dot{R}U - U^2}{2} - a\ddot{a} - \frac{3}{2}\dot{a}^2 = \frac{p_L(R) - p_L(a)}{\rho_L} \tag{4}$$

$$b\ddot{b} + \frac{3}{2}\dot{b}^2 = \frac{p_E(b) - p_\infty}{\rho_E} \tag{5}$$

$$b\ddot{b} - a\ddot{a} + \frac{3}{2}(\dot{b}^2 - \dot{a}^2) = \frac{p_S(a) - p_S(b)}{\rho_S} + \sigma_{rr}^S(a) - \sigma_{rr}^S(b) \tag{6}$$

Where subscripts L, S, E are used to denote properties corresponding to the inner liquid, shell, and outer liquid respectively. p_L and p_E represent the hydrostatic pressure within the inner and outer liquid respectively. The shell is assumed to be a viscoelastic material having both elastic stress and viscous stress terms p_S and σ_{rr}^S. In addition, taking into account surface tensions, viscosities, shell elasticity,

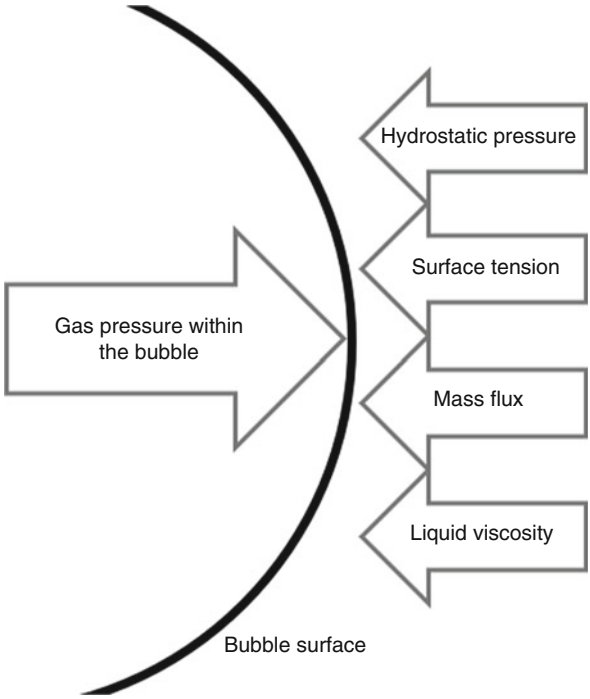

Fig. 2 Normal stress contributions from the outside and within the bubble

as well as the mass flux across the bubble surface, the continuity of normal stress across the bubble surface, shell inner surface, and shell outer surface (Fig. 2) gives the following [1, 6]

$$p_L(R) + JU = p_V(R) - 4\eta_L \frac{U}{R} - 2\frac{\sigma}{R} + JU_V \tag{7}$$

$$p_L(a) = p_S(a) - \sigma_{rr}^S(a) - 4\eta_L \frac{\dot{a}}{a} + \frac{2\sigma_1}{a} \tag{8}$$

$$p_E(b) = p_S(b) - \sigma_{rr}^S(b) - 4\eta_E \frac{\dot{b}}{b} - \frac{2\sigma_2}{b} \tag{9}$$

Where J is the mass flux across the bubble surface, $U_V := \lim_{r \to R^-} u(r,t)$ is the gas velocity at the inner surface of the bubble, η is the dynamic viscosity of the medium denoted by its subscript, and $\sigma, \sigma_1, \sigma_2$ are the surface tensions corresponding to the bubble surface, shell inner surface, and shell outer surface.

Combining Eqs. (4)–(9) results in the generalized Rayleigh-Plesset equation which describes the evolution of the bubble radius over time.

$$\begin{aligned}(R^2\dot{U} + 2R\dot{R}U)\left(\frac{\rho_E - \rho_S}{b} + \frac{\rho_S - \rho_L}{a} + \frac{\rho_L}{R}\right) \\ -\frac{R^4U^2}{2}\left(\frac{\rho_E - \rho_S}{b^4} + \frac{\rho_S - \rho_L}{a^4} + \frac{\rho_L}{R^4}\right) = p_R - p_\infty\end{aligned} \tag{10}$$

Where p_∞ is the pressure at infinity arising from an applied acoustic field as follows.

$$p_\infty(t) = p_0 - p_a \sin(2\pi f t) \tag{11}$$

Where p_0 is the ambient pressure, p_a is the amplitude of the acoustic wave, and f is the acoustic frequency. By the conservation of mass, the mass flux J is given by [3]:

$$J = \rho_L(U - \dot{R}) = \rho_V(U_V - \dot{R}) \tag{12}$$

Given this mass flux, together with Eq. (2), and noting that the shell is impermeable, the differential equations describing the evolution of R, a, b over time are given by.

$$\dot{R} = U - \frac{J}{\rho_L} \tag{13}$$

$$\dot{a} = \frac{R^2}{a^2}U \tag{14}$$

$$\dot{b} = \frac{R^2}{b^2}U \tag{15}$$

2.2 Pressure Contributions

In the process of obtaining Eq. (10), we see that the pressure at the bubble surface p_R can be broken down into contributions from viscosity, surface tension, mass flux, and shell response respectively.

$$p_R = p_V - \frac{2\bar{\sigma}}{R} - \frac{4\bar{\eta}U}{R} + \Phi + \mathcal{S} \tag{16}$$

Where

$$\bar{\eta} = \eta_L + (\eta_S - \eta_L)\left(\frac{R}{a}\right)^3 + (\eta_E - \eta_S)\left(\frac{R}{b}\right)^3 \tag{17}$$

$$\bar{\sigma} = \sigma + \frac{\sigma_1}{a} + \frac{\sigma_2}{b} \tag{18}$$

p_V is the pressure of the gas within the bubble. It can be determined using the Clausius-Clapeyron relation if the temperature is given (to be discussed in Sect. 2.3).

$$p_V(T) = p_{ref} \exp\left(\frac{L}{r_V}\left(\frac{1}{T_{ref}} - \frac{1}{T}\right)\right) \tag{19}$$

Where L is the latent heat of vaporization, r_V is the specific gas constant, and p_{ref} is the known pressure at a reference temperature T_{ref}

Φ is the contribution from the mass flux terms appearing in Eq. (7)

$$\Phi = J(U_V - U) \tag{20}$$

Using Eq. (12), this can be re-expressed as

$$\Phi = J^2\left(\frac{1}{\rho_V} - \frac{1}{\rho_L}\right) \tag{21}$$

The mass flux J itself is obtained from the conservation of energy across the bubble surface [4], assuming that the temperature distribution is uniform within the bubble (Sect. 2.3).

$$J = -\frac{K_L}{L}\frac{\partial T}{\partial r}\Big|_{r \to R^+} \tag{22}$$

Where K_L is the thermal conductivity of the inner liquid.

$\mathcal{S}$ is the contribution from the shell response which will be discussed in Sect. 2.4.

2.3 *Temperature Profile*

The determination of the pressure within the gas bubble within Eq. (19) as well as the mass flux across the bubble surface (22) requires the temperature within the bubble, as well as the temperature gradient immediately outside the bubble.

2.3.1 Bubble Surface Temperature

The modelling of the bubble surface temperature requires the determination of the gas velocity field within the bubble. This begins by assuming that it behaves as an ideal gas. The corresponding enthalpy equation is as follows [2]

$$\rho_V C_p \frac{dT}{dt} - \frac{dp}{dt} = \nabla \cdot (K_V \nabla T) \tag{23}$$

Where ρ_V is the gas density, C_p is its heat capacity under constant pressure, $T := T(r, t)$ is its temperature, and K_V is its thermal conductivity. The gas velocity field within the bubble $\vec{v}$ is introduced through the continuity equation.

$$\frac{\partial \rho_V}{\partial t} + \nabla \cdot (\rho_V \vec{v}) = 0 \tag{24}$$

The following ideal gas property is also used

$$C_p \rho_V T = \frac{\gamma p}{\gamma - 1} \tag{25}$$

Where $\gamma := \frac{C_p}{C_v}$ is the ratio of the specific heat at constant pressure to the specific heat at constant volume. Combining Eqs. (23)–(25), keeping in mind the assumption that the vapor density is constant in space, the following differential equation is obtained.

$$\frac{dp}{dt} + \gamma p \nabla \cdot \vec{v} = (\gamma - 1) \nabla \cdot (K_V \nabla T) \tag{26}$$

This is re-expressed as follows using the assumption of spherical symmetry.

$$\frac{\partial (r^2 v)}{\partial r} = \frac{r^2}{\gamma p} \left[\frac{\gamma - 1}{r^2} K_V \frac{\partial}{\partial r} \left(r^2 \frac{\partial T}{\partial r} \right) - \dot{p} \right] \tag{27}$$

Which is integrated to obtain the vapor velocity field within the bubble

$$v = \frac{1}{\gamma p} \left[(\gamma - 1) K_V \frac{\partial T}{\partial r} - \frac{r \dot{p}}{3} \right] \tag{28}$$

We know that $U_V = \lim_{r \to R^-} v(r, t)$. In addition, since the temperature field within the bubble is assumed to be spatially uniform, this reduces to

$$U_V = -\frac{R \dot{p}}{3 \gamma p} \tag{29}$$

Which can be plugged into the combination of Eqs. (12) and (22) to obtain

$$R \dot{p} + 3 \gamma p \left(\dot{R} - \frac{1}{\rho_V} \frac{K_L}{L} \frac{\partial T}{\partial r} \Big|_{r \to R^+} \right) = 0 \tag{30}$$

The Clausius-Clapeyron relation given in Eq. (19) provides the time rate of change of pressure, which is then used to obtain the final differential equation governing the

evolution of bubble surface temperature (hereby denoted T_S) over time.

$$\frac{L}{r_v T_S^2}\frac{dT_S}{dt} = \frac{3\gamma}{R}\left(\frac{K_L}{\rho_V L}\frac{\partial T}{\partial r}\Big|_{r\to R^+} - \dot{R}\right) \tag{31}$$

Where the gas density ρ_V can be obtained from the following ideal gas relation.

$$\rho_V = \frac{p_V}{r_V T} \tag{32}$$

2.3.2 Temperature Within the Inner and Outer Liquids

The temperature profiles within the inner and outer liquids are given by the energy equations [4, 7]

$$\frac{\partial T}{\partial t} + u(r,t)\frac{\partial T}{\partial r} = \frac{D_m}{r^2}\frac{\partial}{\partial r}\left(r^2\frac{\partial T}{\partial r}\right) + \frac{12\eta_m}{\rho_m c_m}\left(\frac{u(r,t)}{r}\right)^2 \tag{33}$$

Where $m \in \{L, E\}$ represents the medium for which the temperature profile is being evaluated and $D := \frac{K}{\rho c}$ is the thermal diffusivity. The heat flux is assumed to be continuous across the shell.

$$K_L\frac{\partial T}{\partial r}\Big|_{r\to a^-} = K_E\frac{\partial T}{\partial r}\Big|_{r\to b^+} \tag{34}$$

And the other boundary conditions are given by the temperature of the bubble surface and the temperature at infinity, which is held constant.

$$\lim_{r\to R^+} T(r,t) = T_S(t) \tag{35}$$

$$\lim_{r\to\infty} T(r,t) = T_\infty \tag{36}$$

2.4 Shell Contribution

In this review we cover two approaches to modelling the pressure term contributed by the shell's response—the Kelvin-Voigt model utilized in Guédra and Coulouvrat [4], and a later model by Lacour, Guédra and Coulouvrat [5] that models the shell as a hyperelastic material using the Mooney-Rivlin strain energy density function to incorporate nonlinear effects that arise as a result of large deformations.

The Kelvin-Voigt model represents the radial component of the viscous stress tensor that appears in Eqs. (6), (8), and (9) as follows

$$\sigma_{rr}^{S}(r) = -4\frac{a^2}{R^3}\left(G_S\frac{a}{3}\left[1-\frac{R_{10}^3}{R_1^3}\right]+\eta_S\frac{\dot{R}_1}{R_1}\right) \tag{37}$$

Where G_S is the shear modulus of the shell and η_S the shear viscosity. This gives the following expression as the shell response

$$\mathcal{S} = -\frac{4}{3}G_S\left(1-\frac{R_{10}^3}{R_1^3}\right)\left(1-\frac{R_1^3}{R_2^3}\right) \tag{38}$$

The Mooney-Rivlin model begins with Mooney's constitutive relation [34]

$$\Psi \approx \frac{G_S}{4}[(1+\beta)(I_1-3)+(1-\beta)(I_2-3)] \tag{39}$$

Where Ψ is the strain energy density function, G is the shear modulus, β is a fitting parameter, and I_1 and I_2 are the first two invariants of the left Cauchy-Green tensor $b = FF^T$. By expressing the two invariant terms in terms of the principal stretch $\lambda := \frac{r}{r_0}$, the strain energy density function can be reexpressed as

$$\Psi \approx \frac{G_S}{4}\sum_{i=-1}^{1}(1+i\beta)\left(\lambda^{-4i}+2\lambda^{2i}-3\right) \tag{40}$$

The shell response can be placed in the following form.

$$\mathcal{S} = \int_{\frac{a}{a_0}}^{\frac{b}{b_0}}\frac{\Psi'(\lambda)}{\lambda^3-1}d\lambda \tag{41}$$

Which can then be integrated to obtain

$$\mathcal{S} = G_S\left[\sum_{i=-1,i\neq 0}^{1}\sum_{k=0}^{1}\frac{1+i\beta}{-i-3k}\lambda^{-i-3k}\right]_{\frac{a}{a_0}}^{\frac{b}{b_0}} \tag{42}$$

3 Numerical Implementation

The set of equations in the previous section can be consolidated into a model of the four main state variables $U, R, a,$ and b. The mass flux J is implicated in multiple sites within the model and its evaluation in turn requires the modelling of the temperature profile $T(r,t)$ of the system. To that end, the spatial terms within

the energy equation (33) are discretized using centralized finite differences. The following variable substitutions were also carried out to keep the boundary points fixed [3].

$$x = \frac{r - R}{a - R}; \forall r \in (R, a) \tag{43}$$

$$y = \frac{l}{r - b + l}; \forall r \in (b, \infty) \tag{44}$$

Where

$$l = B\sqrt{\frac{D_E}{\omega}} \tag{45}$$

B being a chosen parameter.

The internal and external liquids were discretized evenly into M and N spatial points respectively. I.e.

$$\forall i \in \{1, \ldots, M\}; x_i = i\Delta x; \text{ where } \Delta x = \frac{1}{M} \tag{46}$$

$$\forall j \in \{1, \ldots, N\}; y_j = j\Delta y; \text{ where } \Delta y = \frac{1}{N} \tag{47}$$

This results in a system of ODEs describing the evolution of temperature at $\{x_1, \ldots, x_M\}$, and $\{y_1, \ldots, y_N\}$. This system needs to be completed with boundary and initial conditions at $r = R \Leftrightarrow x_0 = 0$ and $r \to \infty \Leftrightarrow y_0 = 0$. The evolution of the bubble surface temperature is described by Eq. (31). By discretizing

$$\left.\frac{\partial T}{\partial r}\right|_{r \to R^+} \approx \frac{T(x_1, t) - T(x_0, t)}{\Delta x} \tag{48}$$

And rearranging Eq. (31), the evolution of bubble surface temperature can also be expressed as a function of the current temperature profile.

$$\frac{dT_S(t)}{dt} = \frac{\partial}{\partial t} T(x_0, t) \approx \frac{3T(x_0, t)^2 r_v \gamma}{LR} \left(\frac{K_L}{\rho_V L} \frac{T(x_1, t) - T(x_0, t)}{\Delta x} - \dot{R} \right) \tag{49}$$

On the other hand, the temperature at infinity is held constant, so

$$\frac{\partial}{\partial t} T(y_0, t) = 0 \tag{50}$$

The continuity of heat flux across the shell described in Eq. (34) was implemented by introducing an additional variable $T_{shell}(t)$ used to obtain the central finite

differences approximating the one-sided derivatives in Eq. (34).

$$\left.\frac{\partial T}{\partial r}\right|_{r\to a^-} = \frac{\partial}{\partial x}T(x_M,t) \approx \frac{T_{shell}(t) - T(x_{M-1},t)}{2\Delta x} \tag{51}$$

$$\left.\frac{\partial T}{\partial r}\right|_{r\to b^+} = \frac{\partial}{\partial y}T(y_N,t) \approx \frac{T(y_{N-1},t) - T_{shell}(t)}{2\Delta y} \tag{52}$$

$T_{shell}(t)$ can then be calculated at each time step by plugging the above into Eq. (34).

To avoid potential numerical difficulties [4], the initial temperature profile is interpolated between the initial bubble surface temperature and the temperature at infinity as follows [24]:

$$T(r,0) = T(\infty,0) - [T(\infty,0) - T_S(0)]\exp\left(-\frac{r - R(0)}{\delta - R(0)}\right) \tag{53}$$

Where δ was chosen to be within $[R(0), 2R(0)]$. The initial bubble surface temperature was obtained by applying the Clausius-Clapeyron relation to the initial pressure, which in turn was the combination of the ambient pressure and the Laplace pressure arising from the surface tension of the interfaces within the system.

$$T_S(0) = \left[\frac{1}{T_{ref}} - \frac{r_V}{L}\ln\left(\frac{p_0 + \frac{2\sigma}{R(0)} + \frac{2\sigma_1}{a(0)} + \frac{2\sigma_2}{b(0)}}{p_{ref}}\right)\right]^{-1} \tag{54}$$

The evolution of the entire system can then be expressed in the following form.

$$\frac{d}{dt}\begin{bmatrix} T(x_0,t) \\ T(x_1,t) \\ \vdots \\ T(x_M,t) \\ T(y_N,t) \\ \vdots \\ T(y_1,t) \\ T(y_0,t) \\ U \\ R \\ a \\ b \end{bmatrix} = f\left(\begin{bmatrix} T(x_0,t) \\ T(x_1,t) \\ \vdots \\ T(x_M,t) \\ T(y_N,t) \\ \vdots \\ T(y_1,t) \\ T(y_0,t) \\ U \\ R \\ a \\ b \end{bmatrix}, p_\infty(t)t\right) \tag{55}$$

This was then solved using the numerical method implemented by *ode15s* within Matlab® [35].

Table 1 Parameters used within the simulations

	Unit	PFP [25–27]	Shell [6]	H_2O
K	W/m K	0.056		0.6
ρ	kg/m^3	1590	1100	998
c	J/kg K	1046		4200
η	mN s/m^2	0.64	0.05	0.001
r_V	J/kg K	28.8		
L	kJ/kg	88		
γ		1.05		

4 Preliminary Results

4.1 Parameters

The physical properties of PFP, the shell material, and the external water are listed in the following Table 1.

The additional parameters involved include the vapor pressure of PFP at the reference temperature of 25 °C, $P_{ref} = 83.99$ kPa [27]. The ambient temperature and pressure were chosen as $T_\infty = 37$ °C, $P_0 = 1$ atm. B, the parameter used in the variable transformation of radial distance external to the encapsulated droplet shown in Eq. (45), was chosen to be 10. δ the parameter involved in setting up the initial temperature profile was chosen to be $1.1R(0)$. σ, the surface tension coefficient of th bubble was 0.0095 N/m. The surface tension coefficients corresponding to the shell inner and outer surfaces were assumed to be 0. β, the fitting parameter appearing in Eq. (39) was chosen to be 1.

The results (Figs. 3 and 4) exhibit two possibilities for the system: continued expansion through induced droplet vaporization, and bubble collapse. It appears that a larger amplitude of the driving acoustic wave imparts more energy into the system and bring it closer to vaporization. A stiffer shell with a higher shear modulus also provides more resistance acting against the bubble expansion, thus increasing the ADV threshold. The effect of nonlinearity introduced by the Mooney-Rivlin model also gives rise to a larger shell response and hence further increasing the energy required for ADV.

5 Conclusion

Acoustic droplet vaporization (ADV) is a mechanism that holds great promise for potential clinical applications ranging from contrast agents in ultrasound, to the administration of drug cargos at specific target sites. The development of appropriate mathematical models can lead to a deeper understanding of the mechanisms and factors involved in the ADV process. Although both models discussed in this paper are based on the Rayleigh-Plesset equation—the models used different constitutive

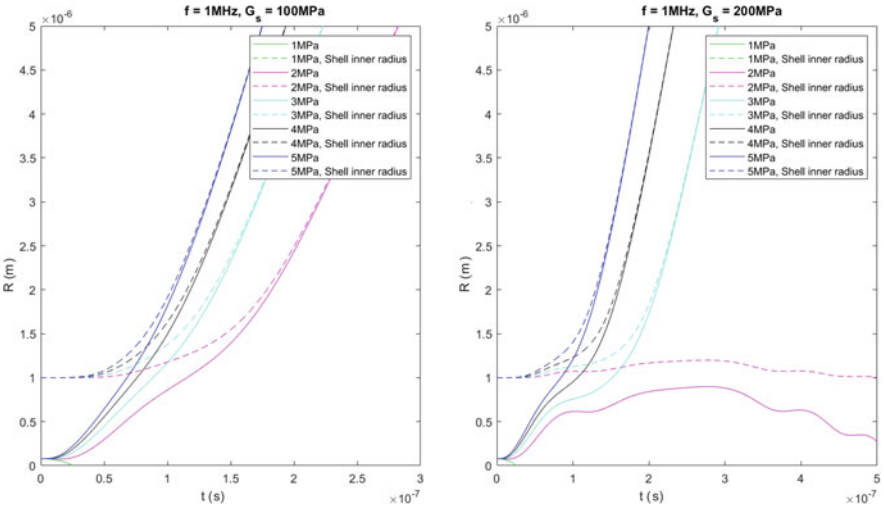

Fig. 3 Evolution of vapor bubble radius and shell inner radius as given by the linear elasticity model under varying amplitudes of the acoustic waves (1 to 5 MPa) and two different shell conditions: left) $G_S = 100$ MPa, and right) $G_S = 200$ MPa

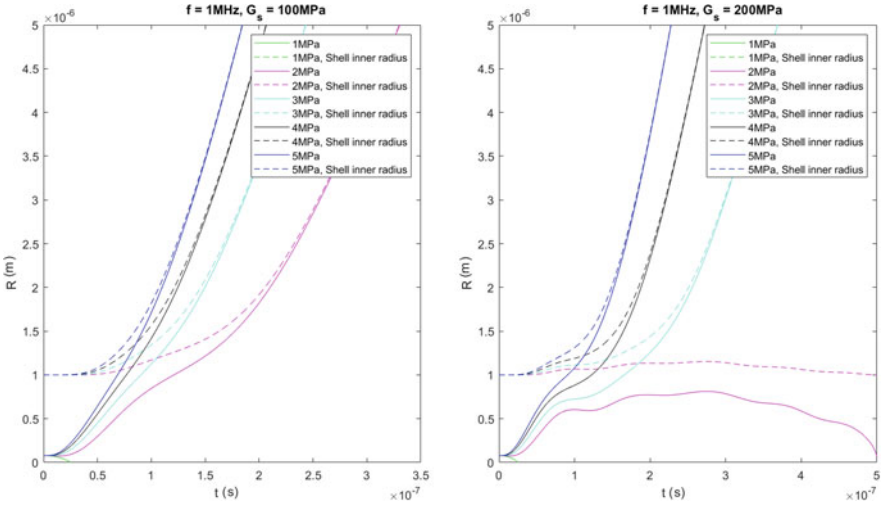

Fig. 4 Evolution of vapor bubble radius and shell inner radius as given by the nonlinear elasticity model under varying amplitudes of the acoustic waves (1 to 5 MPa) and two different shell conditions: left) $G_S = 100$ MPa, and right) $G_S = 200$ MPa

equations. The first model uses linear elasticity theory, whilst the second utilizes a Mooney-Rivlin model that is more suitable for large shell deformations. These models can be used to develop some understanding of the mechanisms that drive the ADV process, as well as to determine key factors in the vaporization process. The

main purpose of this paper is to present and compare these two models presented in the literature to study the ADV process.

Acknowledgments Work partially supported by an NSERC CREATE Grant and Discovery Grants (AY, SS) from the National Science and Engineering Research Council, Canada.

References

1. A. Prosperetti, *Meccanica* **14**, 34 (1979).
2. A. Prosperetti, *J. Fluid. Mech.* **222**, 587 (1991).
3. Y. Hao and A. Prosperetti, *Phys. Fluids* **11**, 2008 (1999).
4. M. Guédra and T. Valier-Brasier, F. Coulouvrat, *J. Acoust. Soc. Am.* **138**, 3656 (2015).
5. T. Lacour, M. Guédra, T. Valier-Brasier, F. Coulouvrat *J. Acoust. Soc. Am.* **143**, 23 (2018).
6. C. Church, *J. Acoust. Soc. Am.* **97**, 1510 (1995).
7. L. D. Landau and E. M. Lifshitz *Fluid Mechanics* Vol. 6, (1966).
8. F. Forsberg, et. al. *J. Ultrasound Med.* **14**, 949 (1995).
9. C.-Y. Lin and W. G. Pitt *BioMed. Res. Int.* **2013**, 404361 (2013).
10. O. D. Kripfgans, et. al. *Ultrasound Med. Biol.* **26**, 1177 (2000).
11. O. D. Kripfgans, M. L. Fabiilli, P. L. Carson, J. B. Fowlkes *J. Acoust. Soc. Am.* **116**, 272 (2004).
12. E. Pisani, et. al. *Adv. Funct. Mater.* **18**, 2963 (2008).
13. N. Rapoport *WIREs Nanomed. Nanobiotechnol.* **4**, 492 (2012).
14. K. Astafyeva, et. al. *J. Mater. Chem.* **3**, 2892 (2015).
15. N. Rapoport, Z. Gao, A. Kennedy *J. Natl. Cancer Inst.* **99**, 1095 (2007).
16. A. Iyer, G. Khaled, J. Fang, H. Maeda *Drug Discov. Today* **11**, 812 (2006).
17. D. Cosco, E. Fattal, M. Fresta, N. Tsapis *J. Fluorine Chem.* **171**, 18 (2015).
18. M. Zhang, et. al. *Ultrasound Med. Biol.* **36**, 1691 (2010).
19. A. L. Martin, et. al. *Ultrasound Med. Biol.* **38**, 1799 (2012).
20. R. Williams, et. al. *Ultrasound Med. Biol.* **39**, 475 (2013).
21. A. H. Lo, et. al. *IEEE Trans. Ultrason. Ferroelectr.* **54**, 933 (2007).
22. N. Reznik, R. Williams, P. N. Burns *Ultrasound Med. Biol.* **37**, 1271 (2011).
23. M. L. Fabiilli, et. al. *IEEE Trans. Ultrason. Ferroelectr.* **56**, 1006 (2009).
24. O. Shpak, L. Stricker, M. Versluis, D. Lohse *Phys. Med. Biol.* **58**, 2523 (2013).
25. P. S. Sheeran, P. A. Dayton *Curr. Pharm. Des.* **18**, 2152 (2012).
26. A. A. Doinikov, P. S. Sheeran, A. Bouakaz, P. A. Dayton *Med. Phys.* **41**, 102901 (2014).
27. FluoroMed® Perfluoropentane http://www.fluoromed.com/products/perfluoropentane/ (Last viewed Oct 7th, 2021)
28. L. Rayleigh *Lond. Edinb. Dubl. Philos. Mag.* **34**, 94 (1917).
29. M. S. Plesset *J. Appl. Mech.* **16**, 277 (1949).
30. M. S. Plesset, S. A. Zwick *J. Appl. Phys.* **25**, 493 (1954).
31. B. E. Noltingk, E. A. Neppiras *Proc. Phys. Soc. London, Sect. B* **63** 674 (1950).
32. Y. Yasui *J. Phys. Soc. Jpn.* **65** 2830 (1996).
33. J. B. Keller, I. I. Kolodner *J. Appl. Phys.* **27**, 1152 (1956).
34. M. Mooney *J. Appl. Phys.* **11**, 582 (1940).
35. Matlab® R2021a, The MathWorks® Inc., Natick, Massachusetts, USA.